JOM, Vol. 71, No. 10, 2019
https://doi.org/10.1007/s11837-019-03690-7

Cold-Workability and Microstructure Change with β-Phase Stability in High-Strength Ti-Mn Binary Alloys

MOHAMMED K. GOUDA,[1,4] MOHAMED A.H. GEPREEL,[1] KENTA YAMANAKA,[2] HAUKANG BIAN,[2] KOICHI NAKAMURA,[1,3] and AKIHIKO CHIBA[2]

1.—Materials Science and Engineering Department, Egypt-Japan University of Science and Technology, Borg El Arab, Alexandria 21934, Egypt. 2.—Institute for Materials Research, Tohoku University, 2-1-1 Katahira, Aoba-ku, Sendai 980-8577, Japan. 3.—Center for the Promotion of Interdisciplinary Education and Research, Kyoto University, Kyoto 615-8540, Japan. 4.—e-mail: mohamed.kamal@ejust.edu.eg

The effect of manganese content (Mn-content) on the beta phase (β-phase) stability, plastic deformability and mechanical behavior of titanium and (8–18 wt.%) manganese low-cost alloys were investigated. The alloys were produced by electric-arc melting under inert argon atmosphere. Microstructure change during cold rolling was evaluated through x-ray diffraction, scanning electron microscope, transmission electron microscope and electron backscatter diffraction in solution-treated and cold-deformed conditions. The β-phase was predominant in all the alloys under study in addition to very fine ω-phase precipitates, especially in the lower Mn-content alloys. Cold workability of the alloys was initially increased in the low Mn-content alloys and then decreased dramatically in the higher Mn-content alloys. The deformation mechanisms were a combination between dislocation slipping and twinning, with a predominance of twinning in the low Mn-content and slipping in the high Mn-content alloys. Tensile test results showed that an ultra-high-strength alloy of about 1950 MPa was obtained in the high Mn-content alloys after cold deformation.

INTRODUCTION

Titanium and its alloys are excellent candidates in many applications such as automotive, biomedical, structural and aerospace applications.[1–3] Among different Ti alloy types, β-titanium alloys have some notable characteristics such as high strength-to-weight ratios, and excellent cold workability and heat treatability, allowing good control of their mechanical and physical properties.[4–6] Recently, the development of good mechanical properties of β-titanium alloys has been attracting considerable research attention.[7,8] The increase in demand for ultra-high-strength materials gives the opportunity for β-titanium to be advantageous over other materials due to its higher specific strength.

The increase in a material's strength, which is mainly related to the dislocation motion, is essential for obtaining high-strength materials. There are different methods to increase the strength of the material based on impeding dislocation movement, for example, introducing a foreign atom inside the lattice to work as an obstacle for the dislocation motion, which is known as solid solution strengthening. Likewise, applying plastic deformation causes a significant increase in dislocation density. This higher dislocation density will lead to interaction between dislocations, making its movement extremely difficult. Also, the decrease in the grain size and precipitation of secondary phases will lead to difficulty in dislocation motion.[9,10]

Several studies on the strengthening mechanisms in β-titanium alloys have been reported. Wei et al.[11] suggested that interstitial solid solution strengthening by oxygen is the reason for the improvement in the ultimate tensile strength of the β-type, Ti-Nb-Ta-Zr alloy. Okazaki et al.[12] concluded that the strength of Ti-15%Zr-4%Nb-2%Ta-0.2%Pd and Ti-15%Sn-4%Nb-2%Ta-0.2%Pd increases linearly with increasing nitrogen and oxygen contents. They also

 (Published online July 26, 2019)

reported that Sn is more effective than Zr from the point of strength improvement, while Nb, Ta, and Pd are much less effective. Moreover, Dai et al.[13] reported that increased dislocation density and grain refinement by cold rolling are primary reasons for the strength improvement of the Ti-35Nb-9Zr-6Mo-4Sn β-type alloy. Recently, Cho et al.[14] found that an increase in the dislocation density, a decrease in grain size and precipitation of deformation-induced ω-phase result in an increase in the ultimate tensile strength of the Ti-13Mn alloy.

In this study, a series of Ti-Mn binary alloys were designed based on the results that came from our previous study, which pointed out that Mn is one of the alloying elements that positively affect the value of the theoretical strength of titanium alloys using first-principles calculations.[15] Mn was chosen as a β-stabilizing element to reduce the raw materials cost of the alloy, as its cost is low compared with other desirable alloying elements, such as Nb and Mo. The effect of the Mn content on phase constituent and strength was studied and the deformation behavior was extensively investigated. Moreover, the mechanical properties were evaluated using tensile tests.

EXPERIMENTAL PROCEDURE

A series of Ti-Mn binary alloys (namely, 8, 10, 12, 14, 16, and 18 wt.% Mn, nominal composition) were produced from a mixture of high-purity titanium sponge and manganese flakes using an electric-arc furnace under inert atmosphere (ARCAST 200; USA). Each specimen was flipped twice while using the electromagnetic stirrer during melting to ensure compositional homogeneity. Samples were subjected to solution heat treatment at 900°C for 30 min under an argon atmosphere, followed by quenching in ice water. The inductively coupled plasma optical emission spectrometry technique was used to measure the compositions of the alloys of the metallic elements (Ti and Mn). The He carrier fusion infrared adsorption method and the He carrier fusion thermal conductivity method were used to detect the oxygen and nitrogen content, respectively.

Cold workability of the alloys was evaluated via unidirectional cold rolling using a Durston rolling mill (FSM 130; UK) without intermediate annealing. A reduction rate of $\sim$ 0.5%-per-pass was applied at a roller speed equal to 25 rpm. The constituent phases were determined by x-ray diffraction (XRD) using a diffractometer (XRD-6100; Shimadzu, Japan) operating at 30 kV and 30 mA in a 2θ range of 29°–80° with a scan speed of 1.0°/min.

Microstructure investigations were carried out using a scanning electron microscope (SEM: JSM-6010LA; JEOL, Japan), after following the standard procedure for grinding and polishing. Samples for transmission electron microscopy (TEM) were prepared by dry polishing and ion milling. TEM observations were carried out using a JEOL JEM-2000EX with an accelerating voltage of 200 kV. The cold-rolling textures were analyzed by the electron backscattered diffraction (EBSD) technique using field-emission scanning electron microscopy (XL30S-FEG; FEI, USA) equipped with TSL OIM^{TM} software.

Mechanical properties were assessed by tensile tests. The samples were cut from the specimens after 90% cold rolling by a wire electrical discharge machine (HS300; Brother Industries, Japan) so that the tensile axis was parallel to the rolling direction. After cutting, all the surfaces were ground using 3000 grit emery papers, followed by washing and drying. Tensile test specimens were prepared with a plate standard geometry. All the specimens were cut with a total length of 34 mm, gauge length of 10 mm, gauge width of 3 mm, thickness of 1.5 mm and fillet radius of 4.0 mm.

The tests were conducted using a universal testing machine (AG-X plus 100; Shimadzu, Japan) with a cross-head strain rate of approximately 1.6×10^{-5} s^{-1} at room temperature. The tensile tests were performed more than two times, and the average values were determined for each condition.

RESULTS

Phase Change with Mn-Content

The chemical compositions of the produced alloys (see supplementary table) are close to the nominal ones. Therefore, the nominal composition represented by the Mn-content is used hereafter for alloy identification. The phases in the alloys in the solution-treated condition were investigated through XRD and microstructure imaging, as shown in Fig. 1. The β-phase is predominant in all the alloys; however, in the 8Mn alloy, the dark field image combined with the selected area electron diffraction (SAED) pattern of the observed area revealed the presence of a very fine nanosized secondary athermal ω (ω_{ath}) phase formed upon quenching in the β-grains, as shown in Fig. 1b and c.

Plastic Deformation Behavior

The plastic deformation at room temperature of the alloys was evaluated by applying cold rolling. The deformability at room temperature was measured as the maximum reduction in thickness by cold rolling before the appearance of a major crack leading to failure. The results of the measurements of cold workability of the Ti-Mn binary alloys are shown in Fig. 2a. The 8Mn-alloy showed limited plastic workability at room temperature, as the percentage of cold rolling thickness reduction was less than 15% before the appearance of major cracks. However, the 8Mn alloy is known to show excellent hot workability.[16] Interestingly, increasing the Mn-content in the alloys to higher levels (i.e., 10% Mn and above) dramatically improved the

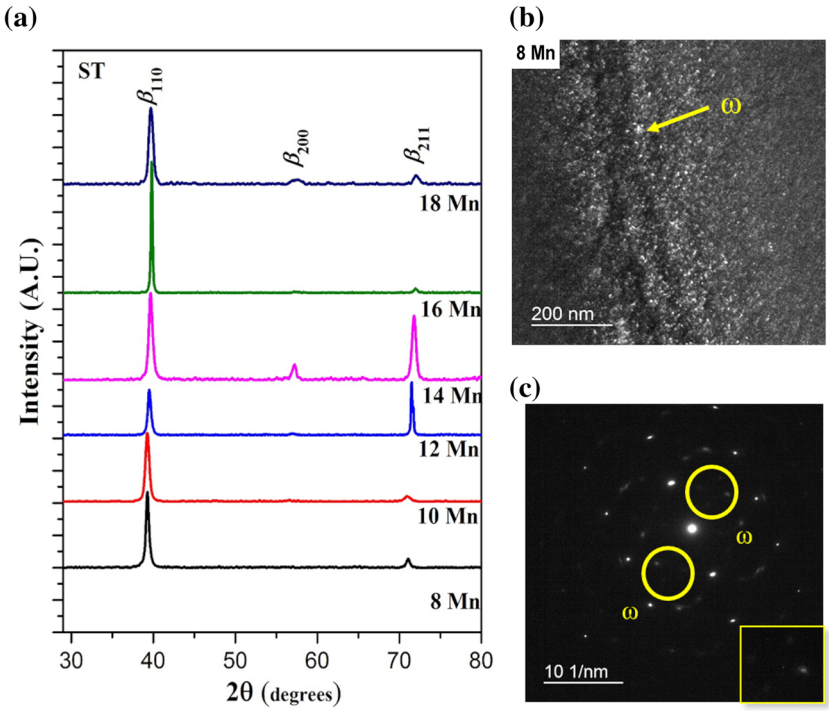

Fig. 1. (a) XRD patterns for Ti-(8-18 wt.%) Mn alloys in solution-treated condition (ST), (b) TEM images of 8Mn alloy (ST) showing dark field and (c) SAED pattern//(110)β.

cold workability: the percent of cold workability increased to more than 90% for the 10Mn alloy. Excellent cold workability more than 90% was also achieved in the 12Mn, 14Mn, and 16Mn alloys, as shown in Fig. 2a. However, the cold workability decreases drastically again to a $\sim$ 10% reduction ratio with a further increase in the Mn-content to 18%. The intermediate alloy composition, 17Mn, showed a transition cold workability of about 15%. In the same way, no cold workability is observed in the 20% Mn-content alloy as the sample was destroyed in the first few passes.[17]

The XRD patterns of the alloys after cold rolling are shown in Fig. 2b, in which it can be seen that in the cold-rolled condition the β-phase is predominant except for some relative intensity change of β-phase XRD peaks. It is known that, after a high degree of cold rolling, the $\{100\}_\beta 100_\beta$ rolling texture is commonly formed due to dislocation movement and grains rotation.[18–20] In this texture, the $\{100\}_\beta$-planes aligned preferably parallel to the rolling plane. As a result, the measured x-ray peak intensity ratio (IR) of the cold rolled specimen (CR), defined as $IR_{CR} = I\{200\}_\beta / I\{110\}_\beta$, changed with cold rolling, where $I\{200\}_\beta$ and $I\{110\}_\beta$ are the x-ray peak intensities of the $\{200\}_\beta$ and $\{110\}_\beta$ reflections, respectively.[18] The IR_{CR} seems to increase with increasing the Mn-content, as shown in Fig. 2b. Also, there are no sign of peaks for any stress-induced transformations even after severe cold rolling, as indicated in the XRD patterns shown in Fig. 2b.

The microstructure observation of the 8Mn alloy at 15%CR is shown in Fig. 2c, in which intergranular cracks and deformation twinning created by cold deformation are shown. However, in the 14Mn alloy, the slipping deformation mechanism can be observed through the formation of many slip/deformation bands, as explained by the arrows.in Fig. 2d.

From the above, it can be concluded that the cold workability and deformation behavior of β-type Ti-Mn binary alloys vary with the Mn-content in the alloy. Poor cold workability is observed in the low β-phase stability alloy with lower Mn-content (8%Mn), followed by excellent cold workability in the intermediate Mn-content (10–16%Mn), and again there is poor cold workability at much higher Mn-content alloys (18Mn and above). Therefore, these compositional ranges will be considered for further investigation to understand the reason(s) for this interesting change in the deformation behavior in this alloy system. The 8Mn, 14Mn, and 18Mn alloys are extensively investigated below using EBSD techniques in addition to TEM observations.

Deformation Behavior Change of the Alloys with Cold Rolling

The microstructures of the three (8, 14, and 18Mn) alloys in the solution-treated condition show equiaxed grains with random orientations, as shown in Fig. 3. On the other hand, some

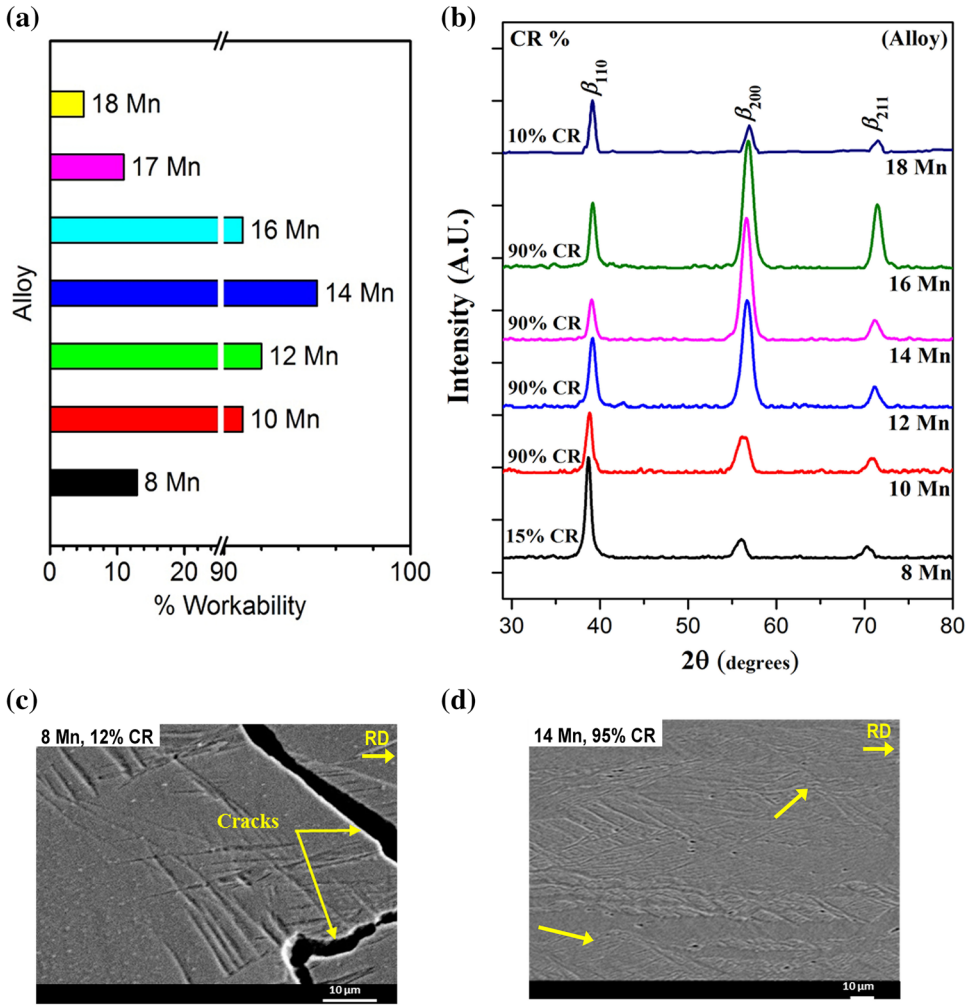

Fig. 2. (a) Cold workability change with Mn-content in binary Ti-Mn alloys (measured from the maximum reduction in thickness by cold rolling without the appearance of major cracks), (b) XRD patterns of the 8–18Mn alloys in the cold-rolled (CR) conditions, (c) SEM image of the 8Mn alloy after 15%CR, and (d) SEM image of the 14Mn alloy in the 95CR condition in a cross-section parallel to the rolling direction.

characteristic features of the deformed alloys are shown in Figs. 4, 5 and 6. The orientation map combined with the image quality for the 8Mn alloy after 10% cold rolling is shown in Fig. 4. The misorientation profiles, which were measured at the locations marked with the yellow lines in Fig. 4a, are shown in Fig. 4b. Moreover, the orientation map combined with the images for the 14Mn and 18Mn alloys after 10% rolling are shown in Fig. 5a and c, respectively.

In Fig. 4a, there are clear observations for slipping traces/bands,as indicated with black arrows in the 10%CR deformed 8Mn alloy. Moreover, there are some bands of fine sub-grains formed at this degree of plastic deformation, as shown in this figure. Also, twinning is induced by deformation, as indicated by the yellow arrows in Fig. 4a. The misorientation line profile technique was used to determine the type of the twin system, as shown in Fig. 4b. It is reported that the coincidence site lattice of the {112}111 twin system corresponds to misorientation of 60° around 111, and 50.57° around 110 for the {332}113 twin systems.[21–23] Therefore, it is confirmed that both of the twinning systems exist with a predominance of the {112}111 twin system, as shown in Fig. 4b. Thus, in the low Mn-content alloy (8Mn) at a low degree of deformation, there is a combination of twinning and slipping deformation mechanisms. However, the twinning mechanism is predominant in the 8Mn alloy and the grain-subdivision (new fine grains) seems to have been initiated at this low degree of deformation. On the other hand, the 14Mn alloy showed relatively different deformation behavior at the same cold rolling reduction ratio (10%), compared to the 8Mn and 18Mn alloys, as shown in Fig. 5a. In this figure, there is a combination of twinning and slipping mechanisms with a predominance of the slipping mechanism. The predominance of slipping, represented by slip/deformation bands, indicated by black arrows in Fig. 5a, is clearer in the 14Mn alloy than at low Mn-content (8Mn) of the same deformation level.

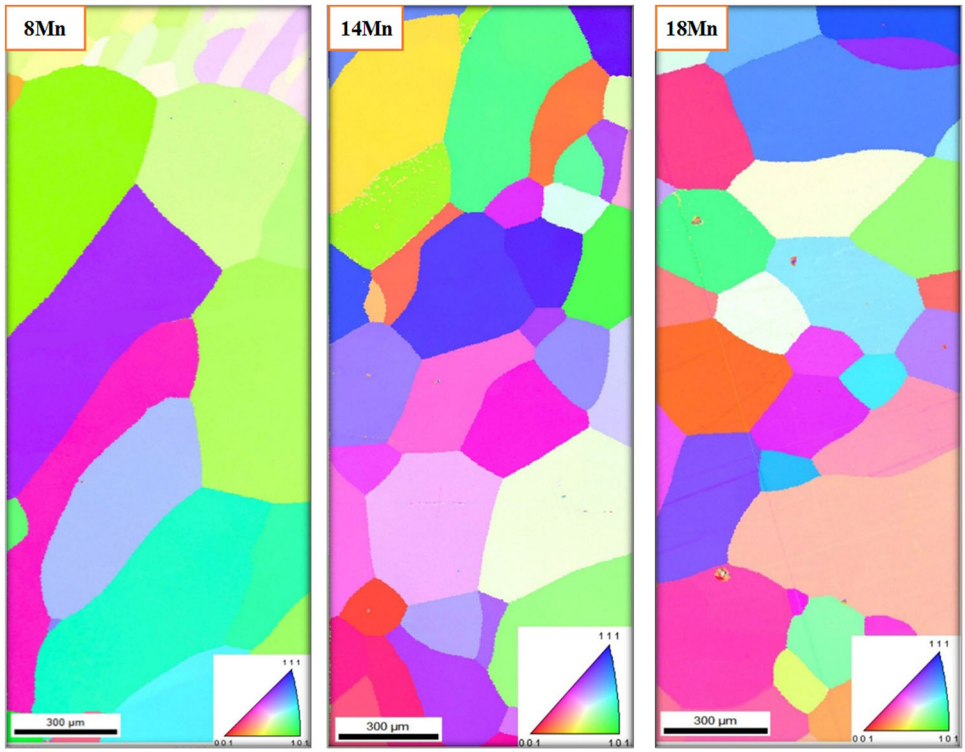

Fig. 3. EBSD orientation map for the (a) 8Mn, (b) 14Mn, and (c) 18Mn alloys in the ST condition.

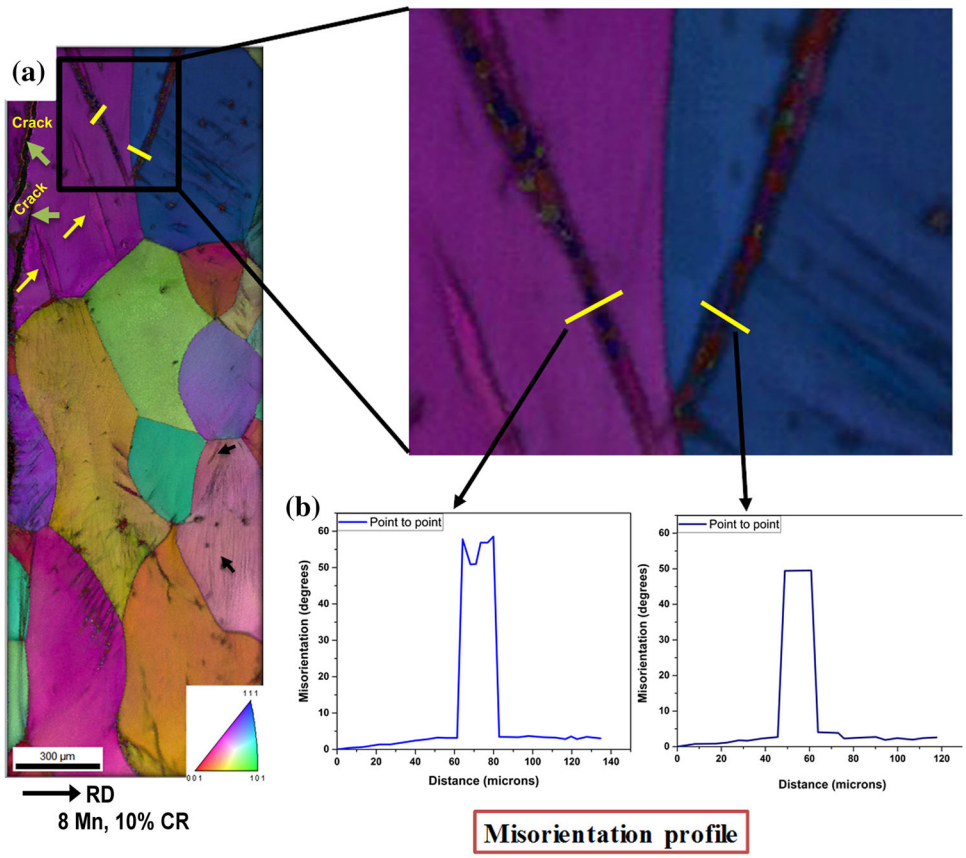

Fig. 4. (a) EBSD orientation map and (b) misorientation profile for line-specified regions for the 8Mn alloy at 10% CR.

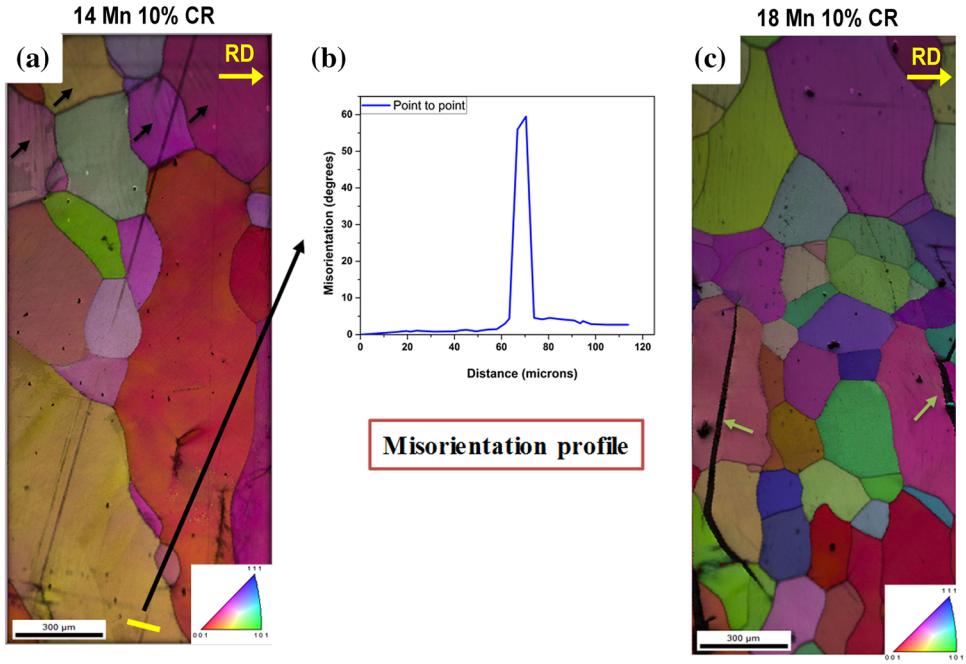

Fig. 5. (a) EBSD orientation map, (b) misorientation profile for line specified regions for the 14Mn alloy at 10% CR and (c) EBSD orientation map for the 18Mn alloy 10% CR.

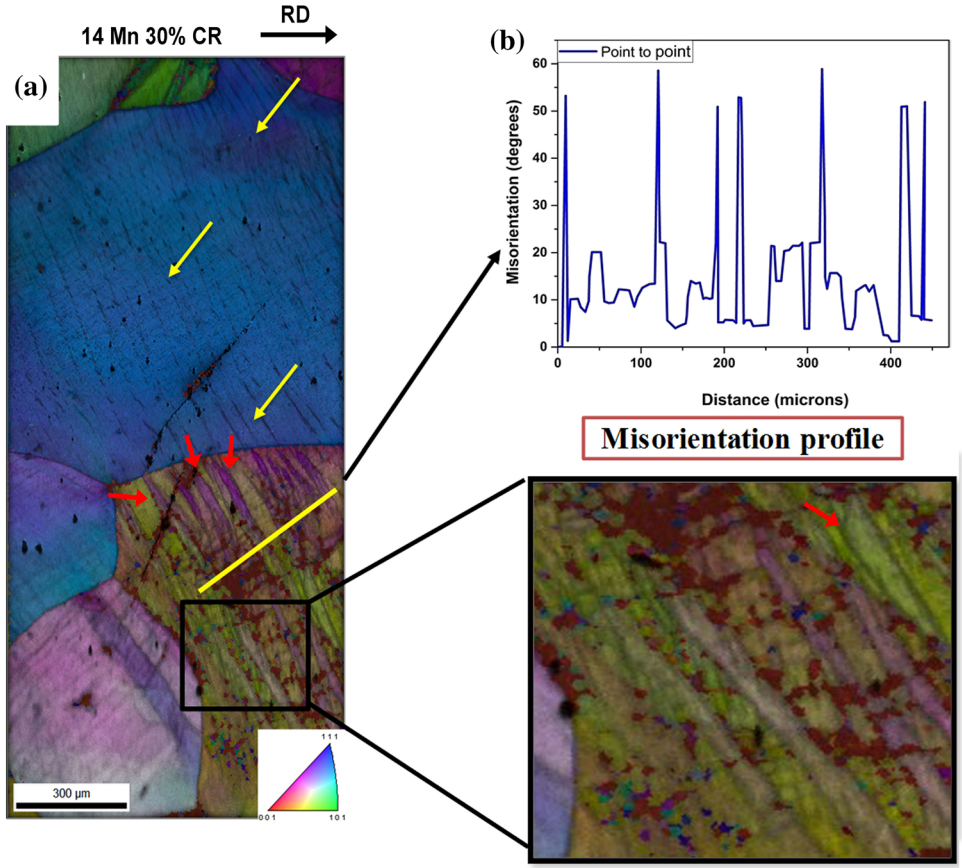

Fig. 6. (a) EBSD orientation map and (b) misorientation profile for line-specified regions for the 14Mn alloy at 30% CR. The red arrows in (a) show an example of the grain subdivisions zone and boundaries with the misorientation angle more than 15°.

Furthermore, in the high Mn-content alloys, the 18Mn alloy showed clear transgranular cracks and traces of deformation/slipping bands at a ~ 10% cold rolling reduction ratio, as shown in Fig. 5c. No evidence for any twinning induced by deformation is observed in the 18Mn alloy.

Deformation Behavior at a Higher Cold Rolling Reduction Ratio

The 14Mn alloy showed excellent cold workability in the Ti-Mn alloy system. Consequently, it will be studied at higher degrees of deformation. Figure 6a introduces the EBSD orientation map with image quality for the 14Mn alloy cold rolled at a 30% reduction ratio. The misorientation profile for the line-specified regions is shown in Fig. 6b, in which the orientation map shows a clear deformation and slipping bands in the alloy after 30%CR, as indicated by the yellow arrows. Also, the misorientation profile shown in Fig. 6b confirms the clear existence of both {112}111 and {332}113 twin systems in the 14Mn alloy at this degree of deformation. Furthermore, grain subdivision at 30%CR can be clearly seen in the 14Mn alloy when compared with the alloy at 10%CR, as indicated by the red arrows in Fig. 6a where the misorientation angles are above 15°.

The Tensile Strength of Cold-Rolled Alloys

After cold rolling up to around 90% reduction ratio, tensile tests were applied on the (10 − 16)Mn alloys along the rolling direction. Values of the measured 0.2% offset yield stress (YS) and ultimate tensile strength (UTS), as well as the plastic stain (strain from yielding to fracture), are shown in Table I.

As shown in Table I, all the alloys showed similar behavior after 90% cold rolling of ultra-high strength with a very small plastic deformation region. In particular, the 14Mn alloy showed an ultimate tensile strength reaching approximately 1950 MPa. The achieved ultra-high tensile strength values after cold rolling of Ti-Mn alloys opens windows for a new ultra-high-strength titanium alloys for different applications such as springs, fasteners, and biomedical applications.

Figure 7 shows the effect of cold rolling on different Ti-Mn alloys. The 8Mn alloy after 15%CR shows both twinning (red arrows) and slipping lines (yellow arrows) in Fig. 7a, while the ω-phase is very clearly observed inside the β matrix, as shown in Fig. 7a by the SAED pattern. The 90%CR 14Mn alloy shows a forest of tangled dislocations and few amounts of the ω-phase Fig. 7b. Although the 14Mn alloy at 90%CR showed low elongation in tensile testing, the fracture surface of the alloy after the tensile test shows ductile dimple fracture and cleavage at ~ 45°, as shown in Fig. 7c and d.

DISCUSSION

From the results, it can be seen that the β-phase is the predominant phase in all the studied Ti-Mn alloys in the solution-treated condition. However, small amounts of nano-sized ω-phase were observed in the low Mn-content alloy (8Mn). Mn is known as a strong β-stabilizing element that suppresses the formation of other metastable phases by quenching from the β-phase. Hence, only the -phase was detected by XRD and there were no signs of the other metastable phases or intermetallic compounds even in high Mn-content alloys (18 and 20%Mn). Therefore, the β-phase stability change of the studied alloys would be in the order 20Mn > 18 Mn > 16Mn > 14Mn > 12Mn > 10Mn. Previous reports[24,25] have mentioned that the Ti-Mn alloy with the least stable single β-phase is at a composition of around 7%Mn-content. However, it seems that 7.36 wt.% Mn (i.e., 8Mn alloy in the present study) is still not enough to retain single β-phase in the alloys as there are minor amounts of ω phase.

After applying 90% cold rolling (90CR) for the Ti-(10-16) Mn alloys, the relative peak intensity ratio, $IR_{CR} = I\{200\}_\beta / I\{110\}_\beta$ IR_{CR} seems to increase with increasing the Mn-content, which is directly related to β-phase stability,[18] as shown in Fig. 2b. Moreover, no stress-induced transformations, such as $\beta \rightarrow \alpha'$, α'' or ω-phases formation, were observed by XRD investigation even after severe cold rolling (i.e., > 90%CR). However, stress-induced $\beta \rightarrow \omega$-phase formation was reported in the Ti-13Mn alloy produced by metal injection molding technique.[14]

As for the deformation mechanism change with β-phase stability in the present alloys, the EBSD testing showed clear signs for both twinning and slipping traces/bands deformation mechanisms at 10% cold rolling ratio in the lower β-phase stability (8Mn) alloy, as shown in Fig. 4a. Grain subdivision

Table I. Values of plastic strain (%), yield strength (YS) and ultimate tensile strength (UTS) (MPa) of 90% cold-rolled Ti-Mn alloys

Sample	Plastic strain (%)	0.2%YS (MPa)	UTS (MPa)
10Mn	0.90 ± 0.02	1755 ± 22	1790 ± 35
12Mn	0.88 ± 0.01	1825 ± 25	1856 ± 37
14Mn	1.35 ± 0.02	1910 ± 20	1945 ± 28
16Mn	1.07 ± 0.04	1870 ± 25	1893 ± 40

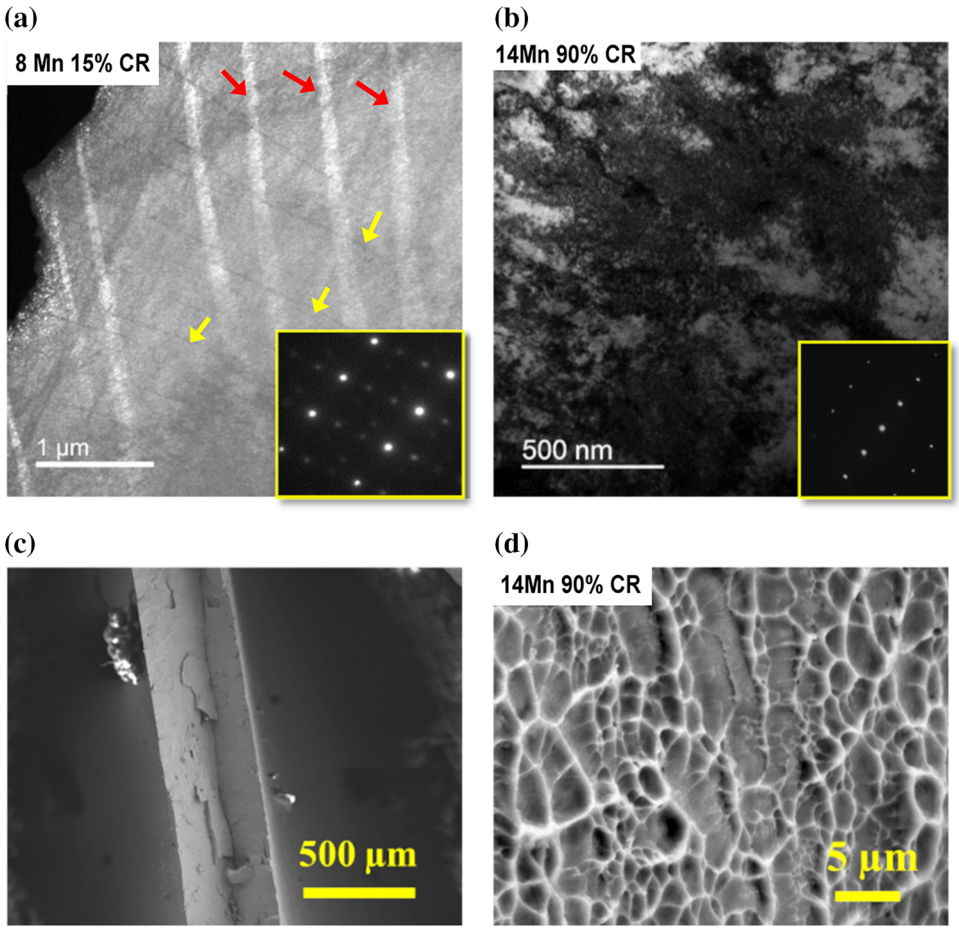

Fig. 7. TEM bright field image for (a) cold-deformed 15%CR 8Mn alloy, (b) 90%CR 14Mn alloy, (c, d) SEM images of the tensile test specimen fracture surface for 14Mn alloy cold deformed 90%CR.

is observed in this lower Mn-content alloy (8Mn) at these early stages of cold rolling reduction ratio where twinning is the dominant deformation mechanism. In addition, significant surface cracks appeared at that low degree of deformation in this lower β-phase stability alloy. However, major cracks appeared by increasing the degree of deformation to 15%CR as indicated in Fig. 4a, and the alloy could not withstand further cold deformation.

The deformation mechanism in the 8Mn alloy at 10%CR is mainly twinning through the activation of both {112}111 and {332}113 twinning systems, probably with a predominance of {112}111. At this level of deformation, grain subdivision is observed where the twinning mechanism is highly activated. It seems that twinned areas support grain subdivision and reorientation. Hence, the formation of subgrains became possible at this level of deformation. However, the presence of the fine ω_{ath}. phase in the grains and at twin boundaries would probably interfere with the deformation process in this alloy, limiting its ability to reach higher deformation levels.

On the other hand, for relatively higher β-phase stability alloys, by increasing the Mn-content (as in 14Mn alloy), the deformation mechanism changes to be mainly slipping as indicated by the appearance of many slipping bands at early stages of deformation (i.e., at 10%CR). Few twins are observed at this level of deformation but no signs for the grain subdivision at this degree of deformation in the relatively higher Mn-content (14Mn) alloy, as seen in Fig. 5a. In conclusion, the deformation mechanism in the 14Mn alloy at 10%CR is a combination of slipping (predominant), mostly through the primary slipping system in the {112}111 direction,[26] and in contrast only the {112}111 twinning system of twinning (predominant) in the 8Mn alloy. Unlike the 8Mn alloy, grain subdivision was not observed at this low degree of deformation in the 14Mn alloy.

In addition, by increasing the degree of deformation to 30%CR in the 14Mn alloy, slipping and twinning deformation mechanisms co-existed in a more explicit way where both {112}111 and {332}113 twin systems are activated in the 14Mn

alloy at this degree of deformation. Therefore, the grain subdivision of 14Mn alloy was also observed at 30%CR condition as observed in the zones with misorientation angles more than 15°, as shown in Fig. 6. It is again concluded that a combination of slipping and twinning deformation mechanisms supports the grain subdivision and the formation of randomly oriented sub-grains in this 14Mn alloy.

However, by increasing the degree of deformation to 90%CR in the 14Mn alloy, this further plastic deformation tends to be accommodated in the form of grain rotation and reorientation where primary/secondary slipping systems could also be activated due to the coexistence of slipping and twinning at this level of deformation. Thus, mainly the {100} atomic plane is preferably aligned parallel to the rolling direction and forms deformation textures as appeared in the XRD patterns. Moreover, the {100}110 rolling texture is commonly observed in many β-type titanium alloys.[27–30]

Nonetheless, for the much higher β-phase stability (i.e., 18Mn alloy) where the electron per atom ratio is higher than low β-phase stability alloys, the cohesive strength of the β bcc lattice would also be higher than lower Mn-content alloys. This is reflected in the elastic and plastic behavior of the alloy.[31–33] Consequently, the higher elastic constants and shear modulus of the high Mn-content alloys, in addition to the absence of the role of twinning in them, will make the material very hard to deform to higher levels of deformation at room temperature.

As shown in Table I, all heavily cold-deformable Ti-Mn alloys showed very high tensile strength after deformation but with low elongation, while the fracture seems ductile in nature, judged from the dimple-like fracture surface of the deformed alloy, as shown in Fig. 7c and d. However, the high degree of cold deformation is considered as the main reason for this low elongation. Notably, the 14Mn alloy showed an ultimate tensile strength of $\sim$ 1950 MPa, which is higher than the known ultra-high-strength titanium alloys, such as Ti-5Al-3Zr-4Cr-4Mo-4V,[34] Ti-20Zr-6.5Al-4V[35] and even Ti-13Mn[14] with UTS values of 1640, 1740 and 1852 MPa, respectively. It is well known that the dislocation motion is the main affecting factor in the different strengthening mechanisms. If the dislocation motion is impeded, higher shear stress is required to overcome their resistance to movement and therefore the material strength increases.

Moreover, the deformation via cold rolling led to a drastic increase in the dislocation density,[14] as observed in Fig. 7. The increase in dislocation density will consequently lead to dislocation interactions, such as dislocation pile-ups and/or dislocation tangles where the dislocations interact with each other, which severely affects their ability to move. This means, that the high degree of cold deformation greatly increased the dislocation density, and therefore an increase in the yield strength of the present alloys are very close to the value of the ultimate tensile strength. In the current study, the TEM observations showing dislocations tangled as a result of the higher dislocation density generated by cold rolling, as shown in Fig. 7b. These observations confirm that dislocation density is playing an essential role in the strengthening of Ti-Mn alloys, as reported previously by Cho et al.[14]

Furthermore, from our previous study based on the first-principles theoretical calculations, the high solid solution strengthening by substituting Ti with Mn is expected in the β-Ti matrix.[15] Moreover, previous reports extensively discussed the effect of O as an interstitial atom on the strength of titanium alloys, particularly alpha and alpha-beta alloys.[36–38] Because of the close oxygen compositional range in the current study, only the effect of solid solution strengthening by Mn alloying will be considered.

In conclusion, the combination of solid solution and plastic deformation strengthening are considered as the main reasons for this high strength value achieved in this cold-rolled Ti-Mn alloys. It is also noticed that yield strength is very close to the ultimate strength. This means that the dislocations are already well tangled by rolling. Therefore, the allowable elongation would be small before cracks appear during the tensile test, but the ductile fracture is still observed.

CONCLUSION

The cold deformability, microstructure, and mechanical properties change with cold deformation of the binary β-type Ti-(8–18 wt.%)Mn alloys are investigated in this study, and the following points are the main conclusions:

- β-phase is the predominant phase in Ti-(8–18 wt.%)Mn alloys, while minor amounts of ω-phase were detected in the low Mn-content alloys in the ST condition, and decreases with increasing the Mn-content in the alloy.
- The binary β-type Ti-Mn alloys deform at room temperature by a combination of twinning and dislocation slipping with a predominance of twinning in the low Mn-content alloys and slipping at higher Mn-content alloys.
- Because of the change in the deformation mechanism with β-phase stability, the high cold workability is limited to a compositional range between 9 and 16% Mn.
- The textured Ti-14Mn alloy showed ultra-high strength up to 1950 MPa after 90% cold rolling with low elongation.

ACKNOWLEDGEMENTS

The authors gratefully acknowledge the Ministry of Higher Education (MoHE) of Egypt for providing a scholarship to conduct this study as well as the Japan International Cooperation Agency (JICA). This work is in the frame of the joint ASRT/DST research project.

ELECTRONIC SUPPLEMENTARY MATERIAL

The online version of this article (https://doi.org/10.1007/s11837-019-03690-7) contains supplementary material, which is available to authorized users.

REFERENCES

1. G. Lütjering and J.C. Williams, *Titanium*, 2nd ed. (Berlin: Springer, 2003), pp. 8–12.
2. M.J. Donachie, *Titanium: A Technical Guide*, 2nd ed. (Ohio: ASM international, 2000), pp. 9–16.
3. C. Leyens and M. Peters, *Titanium and Titanium Alloys: Fundamentals and Applications*, 1st ed. (Weinheim: Wiley-VCH, 2005), pp. 37–42.
4. O.M. Ivasishin, P.E. Markovsky, S.L. Semiatin, and C.H. Ward, *Mater. Sci. Eng. A* 405, 296 (2005).
5. H. Matsumoto, S. Watanabe, and S. Hanada, *J. Alloys Compd.* 439, 146 (2007).
6. O.M. Ivasishin, P.E. Markovsky, Y.V. Matviychuk, S.L. Semiatin, C.H. Ward, and S. Fox, *J. Alloys Compd.* 457, 296 (2008).
7. S. Zaefferer, *Mater. Sci. Eng. A* 344, 20 (2002).
8. J. Hwang, S. Kuramoto, T. Furuta, K. Nishino, and T. Saito, *J. Mater. Eng. Perform.* 14, 747 (2005).
9. W.D. Callister and D.G. Rethwisch, *Fundamentals of Materials Science and Engineering: An Integrated Approach*, 5th ed. (New York: Wiley, 2012), pp. 206–212.
10. W.D. Callister and D.G. Rethwisch, *Materials Science and Engineering: An Introduction*, 8th ed. (New York: Wiley, 2010), pp. 211–218.
11. Q. Wei, L. Wang, Y. Fu, J. Qin, W. Lu, and D. Zhang, *Mater. Des.* 32, 2934 (2011).
12. Y. Okazaki, S. Rao, S. Asao, T. Tateishi, S. Katsuda, and Y. Furuki, *Mater. Trans. JIM* 39, 1053 (1998).
13. S. Dai, Y. Wang, F. Chen, X. Yu, and Y. Zhang, *Mater. Sci. Eng. A* 575, 35 (2013).
14. K. Cho, M. Niinomi, M. Nakai, H. Liu, P.F. Santos, Y. Itoh, M. Ikeda, M.A.H. Gepreel, and T. Narushima, *J. Alloys Compd.* 664, 272 (2016).
15. M.K. Gouda, K. Nakamura, and M.A.H. Gepreel, *J. Appl. Phys.* 117, 214905 (2015).
16. R. Boyer, G. Welsch, and E.W. Collings, *Materials Properties Handbook: Titanium Alloys, 4th Pr* (Ohio: ASM international, 2007), pp. 755–756.
17. M.K. Gouda, K. Nakamura, and M.A.H. Gepreel, *Key Eng. Mater.* 705, 214 (2016).
18. M. Abdel-Hady, Texturing tendency in β-type Ti-alloys.*Recent Developments in the Study of Recrystallization*, ed. P. Wilson (London: IntechOpen, 2013), p. 117.
19. M. Abdel-Hady and M. Morinaga, *Int. J. Mod. Phys. B* 23, 1559 (2009).
20. M. Abdel-Hady, K. Hinoshita, H. Fuwa, Y. Murata, and M. Morinaga, *Mater. Sci. Eng. A* 480, 167 (2008).
21. H. Liu, M. Niinomi, M. Nakai, and K. Cho, *Acta Biomater.* 24, 361 (2015).
22. E. Bertrand, P. Castany, I. Péron, and T. Gloriant, *Scr. Mater.* 64, 1110 (2011).
23. T. Furuta, S. Kuramoto, J. Hwang, K. Nishino, and T. Saito, *Mater. Trans.* 46, 3001 (2005).
24. I. Weiss and S. Semiatin, *Mater. Sci. Eng. A* 263, 243 (1999).
25. M. Ikeda, M. Ueda, R. Matsunaga, M. Ogawa, and M. Niinomi, *Mater. Trans.* 50, 2737 (2009).
26. Y. Yang, G.P. Li, G.M. Cheng, Y.L. Li, and K. Yang, *Appl. Phys. Lett.* 94, 061901 (2009).
27. T. Inamura, Y. Fukui, H. Hosoda, K. Wakashima, and S. Miyazaki, *Mater. Sci. Forum* 475–479, 2323 (2005).
28. H.Y. Kim, T. Sasaki, K. Okutsu, J.I. Kim, T. Inamura, H. Hosoda, and S. Miyazaki, *Acta Mater.* 54, 423 (2006).
29. L. Wang, W. Lu, J. Qin, F. Zhang, and D. Zhang, *Mater. Sci. Eng. A* 491, 372 (2008).
30. T. Inamura, Y. Kinoshita, J.I. Kim, H.Y. Kim, H. Hosoda, K. Wakashima, and S. Miyazaki, *Mater. Sci. Eng. A* 438–440, 865 (2006).
31. G.P. Tiwari and R.V. Ramanujan, *J. Mater. Sci.* 36, 271 (2001).
32. S. Kuramoto, T. Furuta, J.H. Hwang, K. Nishino, and T. Saito, *Metall. Mater. Trans. A* 37, 657 (2006).
33. T.-K. Jung, S. Semboshi, N. Masahashi, and S. Hanada, *Mater. Sci. Eng. C* 33, 1629 (2013).
34. J.W. Lu, Y.Q. Zhao, P. Ge, H.Z. Niu, Y.S. Zhang, W. Zhang, and P.X. Zhang, *Mater. Sci. Eng. A* 621, 182 (2015).
35. R. Jing, S.X. Liang, C.Y. Liu, M.Z. Ma, and R.P. Liu, *Mater. Des.* 52, 981 (2013).
36. F.H. Froes, *Titanium: Physical Metallurgy, Processing, and Applications*, 1st ed. (Ohio: ASM international, 2015), pp. 59–62.
37. H. Liu, M. Niinomi, M. Nakai, J. Hieda, and K. Cho, *J. Mech. Behav. Biomed. Mater.* 30, 205 (2014).
38. M. Nakai, M. Niinomi, T. Akahori, H. Tsutsumi, and M. Ogawa, *Mater. Trans.* 50, 2716 (2009).